Giant ripples on comet 67P/Churyumov–Gerasimenko sculpted by sunset thermal wind

Pan Jia (贾 攀)[a], Bruno Andreotti[a], and Philippe Claudin[a,1]

[a]Laboratoire de Physique et Mécanique des Milieux Hétérogènes, UMR CNRS 7636/Ecole Supérieure de Physique et Chimie Industrielles Paris–Paris Science Lettres Research University/Université Pierre et Marie Curie–Sorbonne Universités/Université Denis Diderot–Sorbonne Paris Cité, 75005 Paris, France

Explaining the unexpected presence of dune-like patterns at the surface of the comet 67P/Churyumov–Gerasimenko requires conceptual and quantitative advances in the understanding of surface and outgassing processes. We show here that vapor flow emitted by the comet around its perihelion spreads laterally in a surface layer, due to the strong pressure difference between zones illuminated by sunlight and those in shadow. For such thermal winds to be dense enough to transport grains—10 times greater than previous estimates—outgassing must take place through a surface porous granular layer, and that layer must be composed of grains whose roughness lowers cohesion consistently with contact mechanics. The linear stability analysis of the problem, entirely tested against laboratory experiments, quantitatively predicts the emergence of bedforms in the observed wavelength range and their propagation at the scale of a comet revolution. Although generated by a rarefied atmosphere, they are paradoxically analogous to ripples emerging on granular beds submitted to viscous shear flows. This quantitative agreement shows that our understanding of the coupling between hydrodynamics and sediment transport is able to account for bedform emergence in extreme conditions and provides a reliable tool to predict the erosion and accretion processes controlling the evolution of small solar system bodies.

dunes | ripples | comet | outgassing | sediment transport

The OSIRIS imaging instrument on board the ESA's (European Space Agency) Rosetta spacecraft has revealed unexpected bedforms (Fig. 1 and Fig. S1) on the neck of the comet 67P/Churyumov–Gerasimenko (67P) (the Hapi region) (1–3) and on both lobes (Ma'at and Ash regions). Several features suggest that these rhythmic patterns belong to the family of ripples and dunes (4). The bedforms present a characteristic asymmetric profile, with a small steep lee side resembling an avalanche slip face (Fig. 1A and Fig. S1B) and a longer gentle slope on the stoss side, which appears darker in Fig. 1B. Analyses of the available photographs show that their typical crest-to-crest distance is on the order of 10 m (Table S1), and that the surface is composed of centimeter-scale grains (6) (Fig. 2). However, the existence of sedimentary bedforms on a comet comes as a surprise—it requires sediment transport along the surface, i.e., erosion and deposition of particles. When heated by the sun, the ice at the surface of comets sublimates into gas. As gravity is extremely small, $g \simeq 2\,10^{-4}$ m/s^2, due to the kilometer scale of the comet (7, 8), the escape velocity is much smaller than the typical thermal velocity. Outgassing therefore feeds an extremely rarefied atmosphere, called the coma, around the nucleus. This gas envelope expands radially. By contrast, ripples and dunes observed in deserts, on the bed of rivers, and on Mars and Titan (4, 9–13) are formed by fluid flows parallel to the surface, dense enough to sustain sediment transport. The presence of these apparent dunes therefore challenges the common views of surface processes on comets and raises several questions. What could be the origin of the vapor flow exceeding the sediment transport velocity threshold (14, 15)? How could the particles of the bed remain confined to the surface of the comet rather than

being ejected into the coma? Our goal here is to understand the emergence of the bedforms on 67P and to constrain the modeling of dynamical processes in the superficial layer of the comet nucleus.

Outgassing and Comet's Atmosphere

Outgassing takes place in the illuminated part of the comet (16, 17). As ice sublimation requires an input of energy—the latent heat—the vapor flux is controlled by the thermal balance at the surface of the comet (*Materials and Methods*). The power per unit area received from the sun depends, at the seasonal scale, on the heliocentric distance and is modulated by the day–night alternation. The comet radiates some energy back to space with a power related to the surface temperature T_s by Stefan's law. Finally, thermal inertia leads to a storage/release of internal energy over a penetration depth that is meter scale for seasonal variations and centimeter scale for daily variations.

The vapor production rate from outgassing, defined as the product of the vapor density ρ_0 by the outward vapor velocity u_0, has been measured for 67P at different heliocentric distances (18–23) (Fig. 3B). Common models assume that ice sublimation takes place at the surface and produces a radial flow at the thermal velocity (25). This would result in a density ρ_0 an order of magnitude smaller than that necessary to induce a fluid drag force large enough to overcome the threshold for grain motion (discussed below). We suggest that most of the vapor is emitted from subsurface ice and must travel through the porous surface granular layer (Fig. S2). Sublimation makes the ice trapped in the pores recede, releasing unglued grains in the surface that can be eroded. This process should lead to an ice level remaining at a constant distance from the surface,

---

Significance

The recent approach to comet 67P/Churyumov–Gerasimenko by the spacecraft Rosetta has revealed the presence of astonishing dune-like patterns. How can the radial outgassing, caused by heating when passing close to the sun, produce a vapor flow along the surface of the comet dense enough to transport grains? Drawing on the physical mechanisms at work for the formation of dunes on Earth and planetary bodies, we quantitatively explain the emergence and size of these bedforms, which are due to thermal winds. This work involves the understanding of the comet surface processes, especially regarding grain cohesion and grain–fluid interaction. It thus provides more keys to address the timely open question on the growth of planetesimals above the meter scale to form planets.
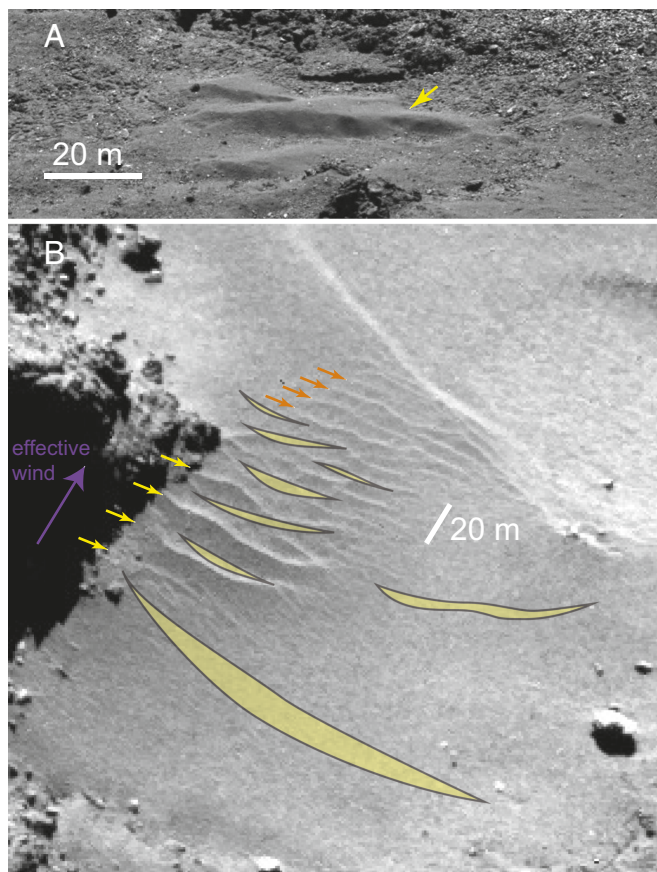

PHYSICS

Fig. 1. Ripples. (*A*) Photograph of ripples in the Maftet region. The central bedform (yellow arrow) has a length $\lambda \simeq 20$ m (Fig. S1*B*) and a height around 2 m, i.e., with a typical aspect ratio 0.1. (*B*) View of the comet's bedforms in the neck (Hapi) region by an OSIRIS narrow-angle camera dated September 18, 2014, i.e., before perihelion. Superimposed yellow marks (*Materials and Methods*): position of the ripples from a photo dated January 17, 2016 (Fig. S1), i.e., after perihelion, providing evidence for their activity. The mean crest-to-crest distance λ ranges from $\simeq 7$ m (emergent ripples upwind of the largest slip face: orange arrows) to $\simeq 18$ m for the larger bedforms (yellow arrows). All photo credits: ESA/Rosetta/MPS, see Table S1 for details.

comparable to the grain size d. Using kinetic theory of gasses, we predict that for such vapor flow the outgassing velocity is 10 times smaller than that of the spectacular vapor jets streaming from active pits (7, 26) (*Materials and Methods*). Accordingly, the vapor atmosphere is 10 times denser than previous estimates.

Altogether, both seasonal and diurnal time variations of the atmosphere characteristics can be obtained in a simplified spherical geometry (Fig. 3 and Fig. S3). At perihelion, we find that the pressure drops by 10 orders of magnitude from day to night (Fig. S3*B*). The comet's atmosphere therefore presents a strong pressure gradient that drives a tangential flow from the warm, high-pressure toward the cold, low-pressure regions, in a surface boundary layer (*Materials and Methods*). The extension of the halo of vapor on the dark side of the comet is a signature of this surface wind (Fig. 4*B*). It reverses direction during the day and is maximal at sunrise and sunset, with a shear velocity u_* on the order of a fraction of the thermal velocity (Fig. 4*A*). The asymmetry between sunrise and sunset simply results from thermal inertia, as some heat is stored in the superficial layer during the morning and released in the afternoon.

Threshold for Grain Motion and Cohesion

The vapor density in the coma is still at most seven orders of magnitude lower than that of air on Earth. Can a surface flow with such density and shear velocity entrain grains into motion? The threshold shear velocity u_t above which sediments are transported by a wind is quantitatively determined by the balance between gravity, hydrodynamic drag, and cohesive contact force (*Materials and Methods*). Investigating this balance highlights the need to apply findings from contact mechanics of rough interfaces (5) to the study of small solar system bodies.
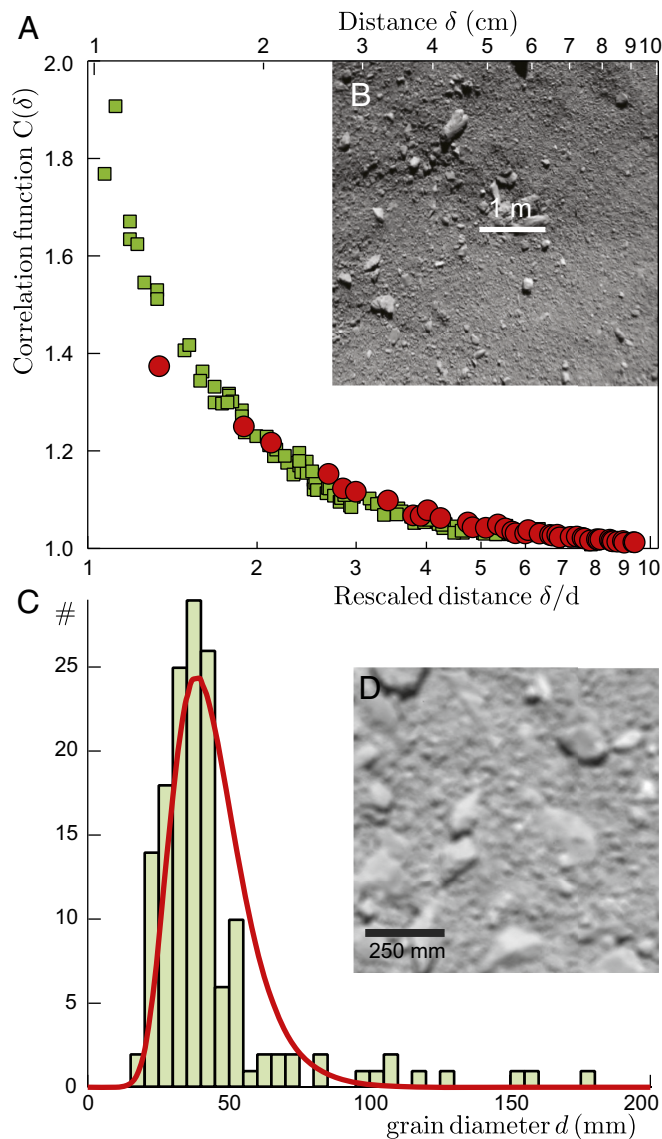

Fig. 2. Grain size. (*A* and *B*) Autocorrelation function $C(\delta)$ (*A*) (red circles) computed from the photograph of the comet's granular bed, taken by Philae just before its touchdown at a site called Agilkia in the Ma'at region (*B*), where large boulders and rocks have been excluded. The resolution of the picture is 9.5 mm/pixel. Photo credit: ESA/Rosetta/Philae/ROLIS/DLR. The correlation is compared with that computed with pictures of calibrated aeolian sand from the Atlantic Sahara (green square, lower axis, δ is expressed in units of the grain diameter) taken in the laboratory (*Materials and Methods*). The best collapse of the correlation functions is obtained for a mean grain diameter $d \simeq 9.7$ mm on the comet. (*C*) Histogram of grain size d computed from the photograph of the comet's granular bed shown in *D* taken by Rosetta just before its impact in the Ma'at region. The best fit by a lognormal distribution, shown in red, gives a mean grain diameter $d \simeq 38$ mm.
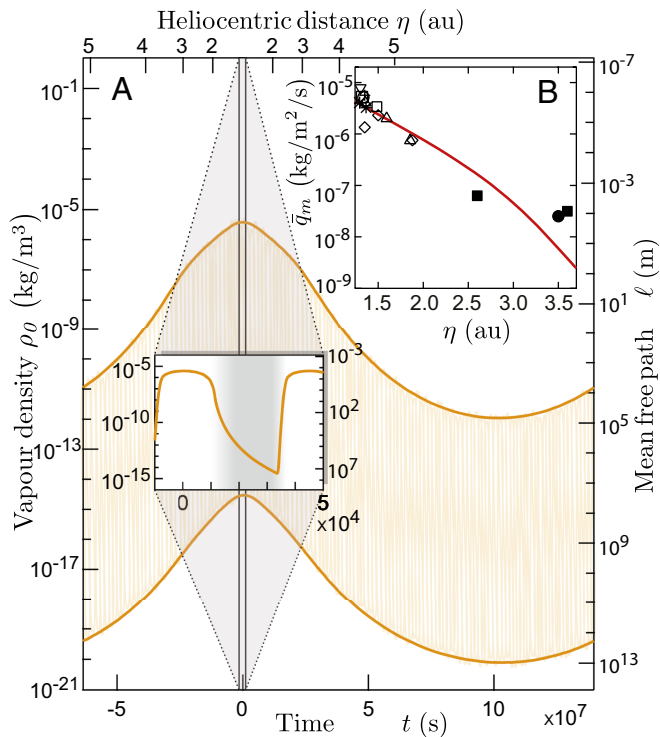
Fig. 3. Vapor density and outgassing. (*A*) Time evolution of the vapor density ρ_0 (left axis) and the corresponding mean free path $\ell \propto 1/\rho_0$ (right axis) just above the comet's surface, calculated along the comet's orbit around the sun in an ideal spherical geometry (*Materials and Methods*). Time is counted with respect to the zenith, at perihelion. Thick orange lines: envelopes of the daily variations (*Inset*), emphasizing the maximum and minimum values. *Inset* shows zoom-in of the time evolution of ρ_0 and ℓ during one comet rotation at perihelion. The day/night alternation is suggested by the background gray scale. (*B*) Global outgassing flux $\bar{q}_m$ as a function of the comet's heliocentric distance η. Solid line: prediction of the model. Symbols: data from the literature: □ from ref. 21; ◇ from ref. 19; △ from ref. 20; *, ▽, and ○ from ref. 23 corresponding to data from 2009, 2002, and 1996, respectively; + from ref. 22; ● from ref. 18; and ■ from ref. 24.

The adhesive free energy, resulting from van der Waals interactions, is proportional to the real area of contact between the grains, which is much smaller than the apparent one because of surface roughness. A realistic computation of this cohesion can be achieved under the assumption that contacts between grains are made of elastically deformed nanoscale asperities and that the apparent area of contact follows Hertz law for two spheres in contact. The cohesive force is then found to scale as the maximal load experienced by the grains to the power $1/3$ (*Materials and Methods*) (27). Considering that this load is typically the weight of a surface grain, this force scales as $(\rho_p g d/E)^{1/3} \gamma d$, where ρ_p is the grain bulk density, E is the grain Young modulus, and γ is the surface tension of the grain material. It is therefore much lower than the force γd obtained for ideally smooth grains. Importantly, the gravity force increases as d^3, whereas the cohesive force increases as $d^{4/3}$ only. This allows us to define a crossover diameter at which these two forces are comparable: $d_m = \left(\gamma^3/E\rho_p^2 g^2\right)^{1/5}$. It gives the typical grain diameter below which cohesive effects become important and are responsible for the increase of the threshold at small d (Fig. 5). On Earth, this diameter for natural grains is around $10\,\mu m$ ([Fig. S4*A*](#)). On 67P, making the simple assumption that the values of E and γ are similar to those on Earth, the value of d_m can be deduced from the gravity ratio to the power $2/5$: $d_m \simeq \left(9.8/2.2\,10^{-4}\right)^{2/5} \times 10\,\mu m \simeq 700\,\mu m$. Such a millimeter scale is three orders of mag-

nitude smaller than the capillary length $\sqrt{\gamma/\rho_p g} \simeq 1\,m$ suggested by traditional approaches, which ignore contact roughness (15).

A second difference from Earth is the large mean free path ℓ of the vapor molecules, which leads to a reduced drag force for grains smaller than ℓ (*Thermo-Hydrodynamics of the Comet's Atmosphere*). This explains that the threshold velocity u_t, plotted as a function of the grain size d (Fig. 5), presents a plateau extending from the millimeter scale to the meter scale (*Materials and Methods*). In conclusion, we find that, sufficiently close to perihelion, all these grains, and in particular those at the centimeter scale observed by Rosetta near bedforms, can be transported by the afternoon thermal wind (Fig. 4). Importantly, this is only a small fraction of the time—typically $\simeq 6.9 \cdot 10^3$ s at perihelion, i.e., $\simeq 15\%$ of the comet's day of 12.4 h. The asymmetry between sunrise and sunset winds has an important consequence: The morning thermal wind is not strong enough to entrain grains.

Emergent Wavelength

Aeolian dunes and subaqueous ripples form by the same linear instability, which is now well modeled and quantitatively tested against laboratory measurements (4). The destabilizing effect results from the phase advance of the wind velocity just above the surface with respect to the elevation profile (Fig. 6*B*). The stabilizing mechanism comes from the space lag between sediment transport and wind velocity. It is characterized by the saturation length L_{sat}, defined as the sediment flux relaxation length toward
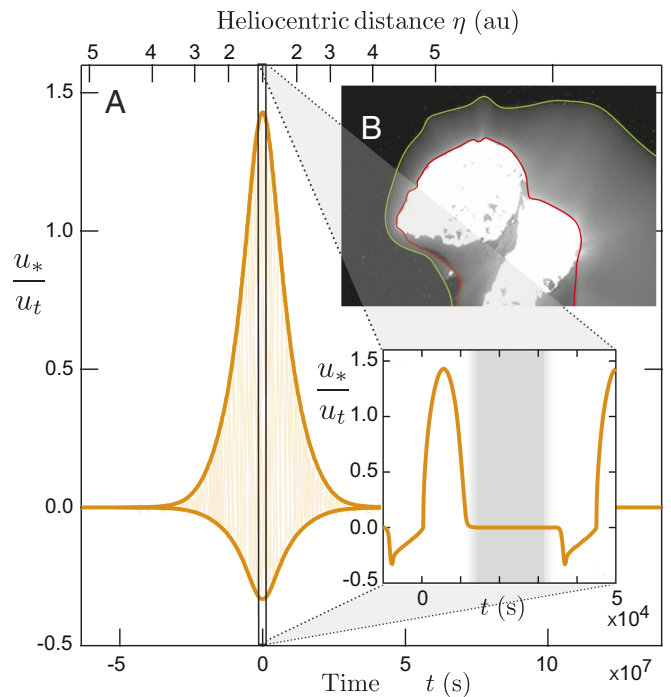

Fig. 4. Winds at sunrise and sunset. (*A*) Time evolution of the velocity ratio u_*/u_t, calculated along the comet's orbit around the sun. Time is counted with respect to the zenith, at perihelion. Thick orange lines: envelopes of the daily variations (*Inset*), emphasizing the maximum and minimum values. *Inset* shows zoom-in of the evolution of u_*/u_t during one comet day, at perihelion. The day/night alternation is suggested by the background gray scale. Wind is above the transport threshold in the afternoon (counted positive) and in the morning (counted negative). (*B*) Picture of the comet and its close coma. Red line shows the contour of the comet. Green line shows the contour of the vapor halo at the resolution of the instrument. Some vapor is present on the dark side of the comet even if the vapor sources are located on the illuminated side, providing evidence for the presence of winds. Image was taken on February 18, 2016, when Rosetta was 35.6 km from the comet, with a resolution of 3.5 m/pixel. Photo credit: ESA/Rosetta/MPS.
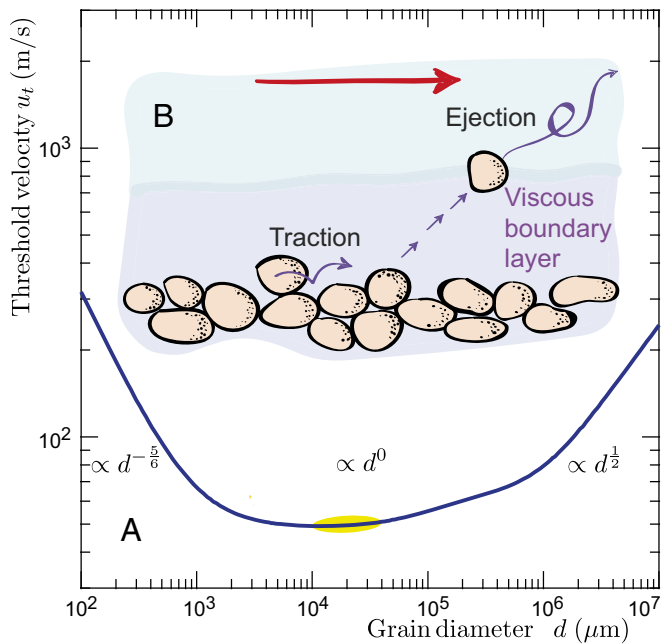
PHYSICS

Fig. 5. Grain motion. (*A*) Dependence of the threshold shear velocity u_t with the grain diameter d at perihelion, for afternoon conditions. The minimal velocity above which sediment transport takes place is computed from the force balance on a grain between hydrodynamic drag, bed friction, and Van der Waals cohesive forces (*Materials and Methods*). The threshold increases above $d \simeq 1$ m due to gravity and below $d \simeq 1$ mm due to cohesion. In between, u_t is almost constant and on the order of 50 m/s due to the large mean free path of the vapor $\ell \simeq 3$ cm. Yellow oval: range of observed grain sizes (Fig. 2). (*B*) Schematic of the vapor flow (red arrow) above the granular bed. Grains rebounding on the bed can reach the upper turbulent zone and are eventually ejected in the coma, which prevents the existence of saltation. The only mode of sediment transport along the bed is traction. Violet background: viscous sublayer close to the bed, typically $10\nu/u_* \simeq 0.7$ m thick close to perihelion.

equilibrium (4, 32, 33). As all other parameters are known, L_{sat} is the key quantity selecting the most unstable wavelength λ. Applying linear stability analysis for 67P (*Materials and Methods*), we compute this wavelength and empirically find that it approximatively scales as $\lambda \approx L_{\text{sat}}^{3/5}(\nu/u_*)^{2/5}$ (Fig. 6*A*).

With the experience of terrestrial deserts, one can recognize the morphology of newborn dunes whose crest-to-crest distance provides a good estimate of λ: They should be sufficiently young not to present a slip face but sufficiently old to be organized into a regularly spaced pattern. Depending on the location, the crest-to-crest distance is measured in the range 5–25 m (Table S1). Making an analogy with sediment transport processes on larger bodies—by transposing scaling laws established for saltation—the analog of aeolian dunes (4, 9, 28) would have an emergent wavelength of 10^8 m due to the extremely large density ratio on the comet, i.e., much larger than the comet itself. Similarly, using the comet's values, the analog for aeolian ripples (29) would produce a pattern of wavelength 10^4 m. As the other elements (asymmetric shape, granular bed, surface wind above transport threshold) do point to bedforms of the dune family, we conclude that the cometary sediment transport is specific and is associated with a saturation length on the order of 10 cm.

Sediment Transport and Bedforms

Given the very large density ratio ρ_p/ρ_0 between grains and vapor, the length needed to accelerate grains to the wind velocity is around 600 km for centimeter-scale grains. This is much larger than the comet size, meaning that the grains actually keep a

velocity u^p negligible in front of the wind velocity u. The moving grains are thus submitted to an almost constant drag force equal to that when the grains are static. We then argue that the mode of sediment transport along the comet's surface is traction, where grains remain in contact with the substratum on which they roll or slide. Traction is a slow mode of transport, where the energy brought by the flow is dissipated during the collision of moving grains with the static grains of the bed. Sediment transport on the comet is therefore analogous to subaqueous bedload (Fig. S5). Adapting Bagnold's approach to the comet (*Sediment Transport*), the sediment flux is proportional to the product of the number of moving grains per unit surface and their mean horizontal velocity (34). In the subaqueous bedload case, because the density ratio ρ_p/ρ_0 is on the order of a few units (in the range 2–4), the moving grains quickly reach a velocity u^p comparable to that of the fluid u. On the comet, the constant mechanical forcing resembles, for the thin transport layer, a granular avalanche, in which dissipation comes from the collisions between the grains and is increasing with u^p (35). In that case, close enough to the threshold, the grain velocity follows the scaling law $u^p \sim \sqrt{gd} \simeq 10^{-3}$ m/s and the density of moving grains is a fraction of $1/d^2$, which means that all of the grains of this surface transport layer move. The corresponding volume sediment flux q_{sat} therefore scales as $q_{\text{sat}} \approx g^{1/2}d^{3/2}$.

In addition to the separation of scales between u^p and u, there are important differences from Earth that prevent a cometary
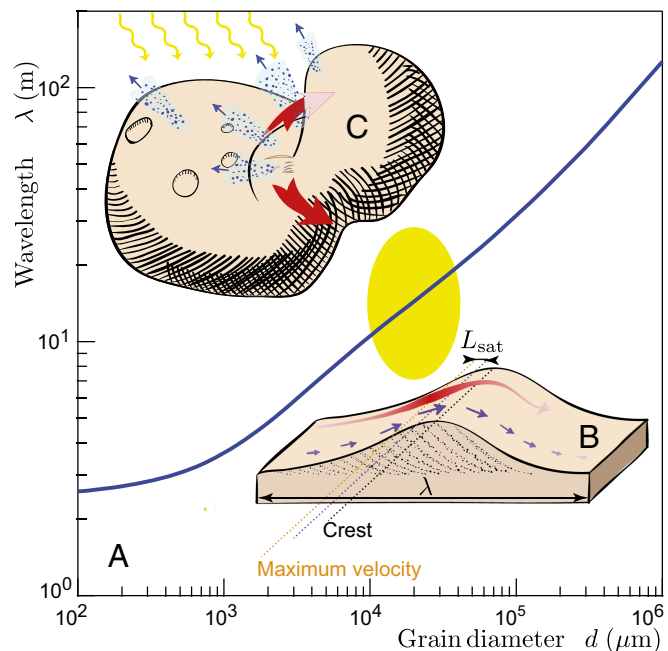

Fig. 6. Ripple wavelength. (*A*) Relation between the wavelength and the mean grain diameter predicted at perihelion, for afternoon conditions. The most unstable mode of the linear instability (*Materials and Methods*) selects the emergent wavelength, which depends on the grain diameter through the saturation length L_{sat} (Fig. S4*B*). Yellow oval: range of measured crest-to-crest distance and grains size (Table S1). (*B*) Schematic of the ripple instability mechanism. The wind velocity close to the surface (red arrow) is modulated by the topography and is maximum (red dotted line) upwind of the crest (black dotted line). The sediment flux, which quantifies the amount of transported grains per unit transverse length and unit time, lags behind the wind velocity by the distance L_{sat}. Grains are eroded (deposited) when the flux increases (decreases). Instability takes place when the crest is in the deposition zone, i.e., when the maximum of the sediment flux (orange dotted line) is upwind of the crest. (*C*) Schematic of the outgassing process (blue) and the resulting winds (red arrows) driven by strong pressure gradients from illuminated to shadow areas.

saltation (3) in which the grains would move by bouncing or hopping (14, 15). The flow is turbulent above a viscous sublayer, typically 0.7 m thick at perihelion, where turbulent fluctuations are damped by viscosity. After a rebound, grains with enough energy to reach the turbulent zone would be entrained into suspension, because the settling velocity is much smaller than turbulent fluctuations (*Sediment Transport*). These grains would acquire a vertical velocity larger than the escape velocity, on the order of 1 m/s, and would eventually be ejected into the coma.

We use here the analogy with subaqueous bedload, for which controlled experiments on emerging subaqueous ripples allow us to deduce $L_{sat}/d \simeq 24 \pm 4$ (Fig. S4B) and retain this law for traction on the comet. As shown in Fig. 6A, for the mean grain diameter d between 10 mm and 40 mm observed in the Ma'at region (Fig. 2), the model predicts an emergent wavelength λ between 10 m and 20 m, in good agreement with the observed crest-to-crest distance (Table S1). For such grains, the traction sediment flux is on the order of $4 \cdot 10^{-5}$ m^2/s. The corresponding ripple growth time deduced from the linear stability analysis is $\simeq 5 \cdot 10^4$ s. This time must be compared with the total time during which sediment transport takes place during a revolution around the sun, which is around 10^6 s (0.7% of the revolution period), i.e., 20 times larger. The ripples therefore have enough time to emerge and mature during one comet revolution. In the neck region, pictures of the same location before and after perihelion (Fig. 1B) provide evidence for ripple activity: The smallest ripples have disappeared at the downwind end of the field and a large one has nucleated at the upwind entrance. In between, ripples may have survived and propagated downwind according to the direction of their slip faces. The displacement predicted by the linear stability analysis, on the order of 10 m (Fig. S6), is consistent with the observed pattern shift (Fig. 1B).

Concluding Remarks

We have argued here that the bedforms observed on 67P are likely to be giant ripples, due to their composition, their asymmetric morphology, and the existence of surface winds driven by the night/day alternation above the transport threshold. These conclusions are reached from a self-consistent analysis but are of course based on limited data. As bedforms reflect the characteristics of the bed and the flow they originate from, they provide strong constraints of the physical mechanisms at work, which challenge alternative explanations. Comets thus provide an opportunity to better understand erosion and accretion processes on planetesimals, with implications for the open question of how these bodies can grow from the meter to the kilometer scale (30, 31).

Materials and Methods

We provide here the main ingredients of our analysis and modeling. *Supporting Information* gives further technical details on the derivation of the model.

Grain Size. Following the technique developed in ref. 9, a series of calibrated photographs of a sand bed is used to relate the image autocorrelation to the mean grain diameter d of the bed, whose value is measured independently by sieve analysis. The reference pictures are taken at resolutions going from 1 pixel to 10 pixels per grain diameter. The rescaled correlation functions $C(\delta)$ corresponding to these pictures at different resolutions collapse on a master curve when δ is divided by d—both expressed in the same units. To determine an unknown mean grain size from a picture whose resolution is known, one computes its autocorrelation $C(\delta)$, with δ expressed in meters or in pixels. One then fits by a least-squares method the value of d that should be used as rescaling factor of δ, to collapse the new curve on the calibration master curve. Even when the grain size is comparable to the resolution, the decay of the correlation between neighboring pixels contains sufficient information to measure d accurately.

Ripple Propagation. Two photographs of the same location—one well before perihelion and the other well after it—were used to estimate the bedform propagation distance over one revolution. The photographs are mapped one on the other, using fixed elements of relief (cliffs, rocks, holes, etc.) that can be recognized on both pictures. The mapping is performed through a projection, assuming in first approximation that the landscape is planar.

Thermal Balance. To determine the surface temperature T_s and the vapor mass flux q_m as a function of time (Fig. 3 and Fig. S3), we solve the power balance per unit surface

$$(1 - \Omega)\psi = \sigma \epsilon T_s^4 + J_s + \mathcal{L} q_m. \qquad [1]$$

This equation relates the solar radiation flux $\psi(t)$ (Ω is the albedo) to the power radiated according to Stefan's law (σ is Stefan's constant and ϵ the emissivity), to the heat diffusive flux J_s toward the center the nucleus, and to the power absorbed by ice sublimation ($\mathcal{L}$ is the latent heat). Heat diffusion in the nucleus is solved analytically, using the decomposition over normal modes in space and time: A mode of frequency ω penetrates exponentially over a depth $\sqrt{2\kappa_c/|\omega|}$, where κ_c is the thermal diffusivity. J_s is therefore related to T_s, through a Fourier transform.

Porous Layer. To determine the outgassing vapor flux q_m, we model the close subsurface as a thin porous granular layer. Water molecules are emitted from the ice surface located below this porous layer and make frequent collisions with the grains, in a way analogous to a chaotic billiard. With a probability close to one, they bounce back and are adsorbed again on the ice surface. The probability to cross the porous layer decreases as the inverse of the porous layer thickness h. Using the kinetic theory of gasses, the average radial velocity u_0 above the layer is determined analytically and corresponds to a Mach number around 0.15. By contrast, with ice directly in contact with the coma, the outgassing Mach number would have been close to 1.

Turbulent Boundary Layer. The pressure gradient along the comet's surface drives a turbulent superficial flow. We model the basal shear velocity u_* associated with this thermal wind, which determines the ability to transport grains along the surface. u_* is related to the surface pressure p_0 and to the outgassing velocity u_0 by the momentum equation integrated over the thickness of the turbulent boundary layer δ_i,

$$\rho_0 |u_*| u_* + \rho_0 \frac{\Lambda}{\kappa} u_0 u_* = -\frac{\delta_i}{2R} \frac{dp_0}{d\theta}, \qquad [2]$$

where $\Lambda \equiv \ln\left(1 + \frac{9u_* \delta_i}{\nu}\right)$ is the logarithm of the Reynolds number based on u_*, δ_i, and the viscosity ν. δ_i is set by the crossover from the inner to the outer layer, i.e., where the inertial terms are comparable to the pressure gradient:

$$\frac{|\Lambda - 2|\delta_i}{2\pi\kappa^2 R} \simeq 1 + \frac{\Lambda}{\kappa} \frac{u_0}{u_*}. \qquad [3]$$

Cohesion Between Grains. The sediment transport threshold depends on the adhesion force A between grains, which is strongly influenced by the grain surface roughness. Considering two grains of diameter d that have been placed in contact by means of a normal load N, the apparent area of contact is governed by Hertz law: $a_a \sim (Nd/E)^{2/3}$, where E is the Young modulus of the material. However, due to the roughness, the real area of contact a_r is much smaller than the apparent one a_a and, according to Greenwood's theory (5), is proportional to the normal load: $a_r \sim N/E$. The adhesion force therefore scales as

$$A \sim \frac{a_a}{a_r} \gamma d \sim \gamma \left(\frac{Nd}{E}\right)^{1/3}. \qquad [4]$$

Sediment Transport Threshold. The shear velocity threshold u_t for sediment transport is computed from the force balance applied on a surface grain on the verge of being entrained into motion. Such a grain is submitted to its weight, to a drag force due to the wind flow, to a cohesive force at the grain contacts, and to a resistive force associated with the geometrical effect of the surrounding grains. The drag force reads $F_{drag} = \pi/8 \, C_d d^2 \rho_0 u^2$, where u is the velocity of the fluid around the grain. The drag coefficient C_d depends on the grain Reynolds number ud/ν to describe both viscous and turbulent regimes. We also include Cunningham's correction to account for the case of a dilute gas, when the mean free path ℓ becomes comparable to the grain size. The grain weight scales as $\rho_p g d^3$ and sets the normal force N in Eq. **4**,

which gives the adhesion force. The resistive force of the bed is modeled as a friction of effective coefficient μ. The expression of u_t can then be derived analytically and takes the form

$$u_t = u_t^0 \left[1 + \left(\frac{d_m}{d} \right)^{5/3} \right]^{1/2}, \qquad [5]$$

where d_m is the cohesive size defined above. In the large d regime, the turbulent drag essentially balances the friction force:

$$u_t \sim \sqrt{(\rho_p/\rho_0)gd} \propto d^{1/2}. \qquad [6]$$

In the intermediate regime for which $d_m < d < \ell$, the viscous drag balances the friction force:

$$u_t \sim \sqrt{(\rho_p/\rho_0)g\ell} \propto d^0. \qquad [7]$$

In the small d regime, the viscous drag balances cohesion:

$$u_t \sim \left(\frac{\rho_p g d}{E} \right)^{1/6} \left(\frac{\gamma \ell}{\rho_p g d^3} \right)^{1/2} \sqrt{(\rho_p/\rho_0)gd} \propto d^{-5/6}. \qquad [8]$$

Linear Stability Analysis. The wavelength λ at which bedforms emerge can be predicted by the linear stability analysis of a flat sediment bed. The growth rate σ and propagation velocity c of a modulated bed are given by

$$\sigma = \mathcal{Q}k^2 \frac{(\mathcal{B} - \mathcal{S}) - \mathcal{A}kL_{\text{sat}}}{1 + (kL_{\text{sat}})^2}, \quad c = \mathcal{Q}k \frac{\mathcal{A} + (\mathcal{B} - \mathcal{S})kL_{\text{sat}}}{1 + (kL_{\text{sat}})^2}. \qquad [9]$$

In these expressions, $k = 2\pi/\lambda$ is the bed wavenumber and $\mathcal{Q}$ is the reference sediment flux. $\mathcal{A}$ and $\mathcal{B}$ are the components of the basal shear stress, respectively, in phase and in quadrature with the elevation profile, which are determined by hydrodynamics (Fig. S7) (4). L_{sat} is the saturation length that reflects the space lag of sediment flux in response to a change of wind velocity. $\mathcal{S}$ encodes the fact that the threshold for transport is sensitive to the bed slope with $\mathcal{S} = \frac{1}{\mu}(u_t/u_*)^2$, where μ is the avalanche slope for the grains considered.

1. Thomas N, et al. (2015) The morphological diversity of comet 67P/Churyumov-Gerasimenko. *Science* 347:aaa0440.
2. El-Maarry MR, et al. (2015) Regional surface morphology of comet 67P/Churyumov-Gerasimenko from Rosetta/OSIRIS images. *Astron Astrophys* 583:A26.
3. Thomas N, et al. (2015) Redistribution of particles across the nucleus of comet 67P/Churyumov-Gerasimenko. *Astron Astrophys* 583:A17.
4. Charru F, Andreotti B, Claudin P (2013) Sand ripples and dunes. *Ann Rev Fluid Mech* 45:469–493.
5. Greenwood JA, Tripp JH (1967) The elastic contact of rough spheres. *J Appl Mech* 34:153–159.
6. Mottola S, et al. (2015) The structure of the regolith on 67P/Churyumov-Gerasimenko from ROLIS descent imaging. *Science* 349:aab0232.
7. Sierks H, et al. (2015) On the nucleus structure and activity of comet 67P/Churyumov-Gerasimenko. *Science* 347:aaa1044.
8. Pätzold M, et al. (2016) A homogeneous nucleus for comet 67P/Churyumov-Gerasimenko from its gravity field. *Nature* 530:63–65.
9. Claudin P, Andreotti B (2006) A scaling law for aeolian dunes on Mars, Venus, Earth, and for subaqueous ripples. *Earth Planet Sci Lett* 252:30–44.
10. Bourke MC, et al. (2010) Extraterrestrial dunes: An introduction to the special issue on planetary dune systems. *Geomorphology* 121:1–14.
11. Fenton L, Ewing RC, Bridges N, Lorenz R (2013) Extraterrestrial aeolian landscapes. *Treatise in Geomorphology*, Aeolian Geomorphology, eds Schroder J, Lancaster N, Baas A, Sherman D (Academic, San Diego), Vol 11, pp 287–312.
12. Lucas A, et al. (2014) Growth mechanisms and dune orientation on Titan. *Geophys Res Lett* 41:6093–6100.
13. Lapotre MGA, et al. (2016) Large wind ripples on Mars: A record of atmospheric evolution. *Science* 353:55–58.
14. Durán O, Claudin P, Andreotti B (2011) On aeolian transport: Grain-scale interactions, dynamical mechanisms and scaling laws. *Aeolian Res* 3:243–270.
15. Kok JF, Parteli EJR, Michaels TI, Karam DB (2012) The physics of wind-blown sand and dust. *Rep Prog Phys* 75:106901.
16. De Sanctis MC, et al. (2015) The diurnal cycle of water ice on comet 67P/Churyumov-Gerasimenko. *Nature* 525:500–503.
17. Filacchione G, et al. (2016) Exposed water ice on the nucleus of comet 67P/Churyumov-Gerasimenko. *Nature* 529:368–372.
18. Gulkis S, et al. (2015) Subsurface properties and early activity of comet 67P/Churyumov-Gerasimenko. *Science* 347:aaa0709.
19. Hanner MS, et al. (1985) The dust coma of periodic comet Churyumov-Gerasimenko. *Icarus* 64:11–19.
20. Osip DJ, Schleicher DG, Millis RL (1992) Comets: Groundbased observations of spacecraft mission candidates. *Icarus* 98:115–124.
21. Schleicher DG (2006) Compositional and physical results for Rosetta's new target comet 67P/Churyumov-Gerasimenko from narrowband photometry and imaging. *Icarus* 181:442–457.
22. Ootsubo T, Kawakita H, Kobayashi H, Usui F, AKARI SOSOS Team (2012) AKARI near-infrared spectroscopic survey for cometary volatiles. *Publ Korean Astron Soc* 27:161–164.
23. Bertaux J-L, Combi MR, Quémerais E, Schmidt W (2014) The water production rate of Rosetta target Comet 67P/Churyumov-Gerasimenko near perihelion in 1996, 2002 and 2009 from Lyman α observations with SWAN/SOHO. *Planet Space Sci* 91:14–19.
24. Bertaux J-L (2015) Estimate of the erosion rate from H_2O mass-loss measurements from SWAN/SOHO in previous perihelions of comet 67P/Churyumov-Gerasimenko and connection with observed rotation rate variations. *Astron Astrophys* 583:A38.
25. Skorov YV, Rickman H (1998) Simulation of gas flow in a cometary Knudsen layer. *Planet Space Sci* 46:975–996.
26. Vincent JB, et al. (2015) Large heterogeneities in comet 67P as revealed by active pits from sinkhole collapse. *Nature* 523:63–66.
27. Restagno F, Crassous J, Cottin-Bizonne C, Charlaix E (2002) Adhesion between weakly rough beads. *Phys Rev E* 65:042301.
28. Elbelrhiti H, Claudin P, Andreotti B (2005) Field evidence for surface-wave-induced instability of sand dunes. *Nature* 437:720–723.
29. Durán O, Claudin P, Andreotti B (2014) Direct numerical simulations of aeolian sand ripples. *Proc Natl Acad Sci USA* 111:15665–15668.
30. Johansen A, et al. (2007) Rapid planetesimal formation in turbulent circumstellar disks. *Nature* 448:1022–1025.
31. Jansson KW, Johansen A (2014) Formation of pebble-pile planetesimals. *Astron Astrophys* 570:A47.
32. Sauermann G, Kroy K, Herrmann HJ (2001) Continuum saltation model for sand dunes. *Phys Rev E* 64:031305.
33. Andreotti B, Claudin P, Pouliquen O (2010) Measurements of the aeolian sand transport saturation length. *Geomorphology* 123:343–348.
34. Durán O, Andreotti B, Claudin P (2012) Numerical simulation of turbulent sediment transport, from bed load to saltation. *Phys Fluids* 24:103306.
35. Andreotti B (2007) A mean-field model for the rheology and the dynamical phase transitions in the flow of granular matter. *Europhys Lett* 79:34001.
36. Cunningham E (1910) On the velocity of steady fall of spherical particles through fluid medium. *Proc R Soc A* 83:357–365.
37. Rotundi A, et al. (2015) Dust measurements in the coma of comet 67P/Churyumov-Gerasimenko inbound to the Sun. *Science* 347:aaa3905.
38. Daerr A (2001) Dynamical equilibrium of avalanches on a rough plane. *Phys Fluids* 13:2115–2124.
39. Abrams J, Hanratty TJ (1985) Relaxation effects observed for turbulent flow over a wavy surface. *J Fluid Mech* 151:443–455.
40. Merrison JP (2012) Sand transport, erosion and granular electrification. *Aeolian Res* 4:1–16.
41. Yalin MS, Karahan E (1979) Inception of sediment transport. *J Hydr Div Proc ASCE* 105(HY11):1433–1443.